Research Square

Preprints are preliminary reports that have not undergone peer review.
They should not be considered conclusive, used to inform clinical practice,
or referenced by the media as validated information.

Color tunability and temperature sensing in transparent Dy3+/Eu3+ co-doped KGd2F7 oxyfluoride glass ceramics

Zhushen Jiang
Ningbo University
Huimin Ding
Ningbo University
Youjun Cai
Ningbo University
Kaikai Ren
Ningbo University
Xin Wang
Ningbo University
Yuepin Zhang
zhangyuepin@nbu.edu.cn
Ningbo University

Research Article

Keywords: Glass-ceramics, KGd2F7, Color tunable emission, Energy transfer, Optical thermometry

Posted Date: August 21st, 2026

DOI: https://doi.org/10.21203/rs.3.rs-10649497/v1

License: This work is licensed under a Creative Commons Attribution 4.0 International License.
Read Full License

Additional Declarations: No competing interests reported.

Color tunability and temperature sensing in transparent Dy^{3+}/Eu^{3+} co-doped KGd_2F_7 oxyfluoride glass ceramics

Zhushen Jiang, Huimin Ding, Youjun Cai, Kaikai Ren, XinWang, Yuepin Zhang*

Key Laboratory of Photo-electronic Materials, Ningbo University, Ningbo, Zhejiang, 315211, China

* Corresponding author, E-mail: zhangyuepin@nbu.edu.cn (Y. Zhang)

Abstract

Transparent oxyfluoride glass-ceramics (GCs) containing KGd_2F_7 nanocrystals co-doped with Dy^{3+} and Eu^{3+} were prepared and systematically studied in terms of their luminescence behavior, energy transfer (ET) mechanism, and ratiometric temperature-sensing performance. X-ray diffraction (XRD) and transmission electron microscopy (TEM) confirmed the uniform precipitation of well-crystallized KGd_2F_7 nanocrystals (~15.7 nm) within the glass matrix. By varying the Eu^{3+} concentration, the emission color was continuously tuned from yellow to orange-red. Efficient $Dy^{3+}\rightarrow Eu^{3+}$ energy transfer via a quadrupole–quadrupole interaction was verified by emission spectra and decay analysis. The optimal sample exhibited an absolute sensitivity (S_a) of 0.372 % K^{-1}, a relative sensitivity (S_r) of 0.388 % K^{-1}, and excellent temperature resolution. These results indicate that the Dy^{3+}/Eu^{3+} co-doped KGd_2F_7 GCs are promising candidates for multicolor displays and high-precision optical thermometry.

Keywords: *Glass-ceramics, KGd_2F_7, Color tunable emission, Energy transfer, Optical thermometry*

1.Introduction:

With the rapid advancement of optoelectronic technologies, including solid-state lighting, flat-panel displays, optical thermometry, and bioimaging, high-performance luminescent materials have become essential for addressing the performance limitations of advanced optoelectronic devices[1-4]. In this context, luminescence efficiency, color tunability, and temperature sensitivity serve as key parameters governing device reliability and practical applicability. Owing to their facile preparation, compositional flexibility, controllable microstructure, high optical transparency, and excellent mechanical and chemical stability, inorganic glasses and glass-ceramics are regarded as promising luminescent hosts. Furthermore, rare-earth ions, with their unique 4f electronic configurations, abundant energy-level transitions, and broad spectral tunability, allow precise control over visible emission, thereby meeting the stringent requirements of high-end displays, customized lighting, and multicolor bioimaging[5, 6].

The composition and microstructure of the host matrix play a crucial role in determining the luminescence properties, energy transfer efficiency, and thermal stability of rare-earth-doped materials. Compared with traditional oxide and phosphate glasses, oxyfluoride GCs combine the low phonon energy of fluorides with the high structural stability of oxide glasses, effectively suppressing non-radiative relaxation and enhancing luminescence efficiency[7-9]. Among various fluoride crystal phases, KGd_2F_7 nanocrystals are particularly attractive because of their low phonon energy, suitable lattice sites for rare-earth ion substitution, and unique self-crystallizing behavior[10]. This host matrix enables the in situ formation of uniformly distributed nanocrystals during the melt-quenching process, eliminating the need for additional crystallization steps while maintaining high optical transparency.

Dy^{3+} and Eu^{3+} ions form a versatile sensitizer-activator pair for efficient energy transfer and precise color tuning. Dy^{3+} acts as a blue/yellow emission center, emitting blue (480 nm) and yellow (575 nm) light, which is favorable for near-white light generation[11]. However, single-doped Dy^{3+} systems commonly exhibit insufficient red

emission and poor color rendering. In contrast, Eu^{3+} acts as an efficient red-emitting activator, compensating for the red-emission deficiency of Dy^{3+} through its intense orange-red emission arising from the $^5D_0 \rightarrow {}^7F_J$ transitions[12-14]. By co-doping Dy^{3+} and Eu^{3+} into a properly designed host matrix, continuous color tuning from yellow to orange-red can be achieved through interionic energy transfer, while also enabling fluorescence intensity ratio thermometry.

The primary objective of this study is to synthesize KGd_2F_7 nanocrystals co-doped with Dy^{3+} and Eu^{3+} ions within oxyfluoride glass-ceramic matrices via a melt-quenching technique followed by subsequent heat treatment. This work aims to systematically investigate the luminescence characteristics of the Dy^{3+}/Eu^{3+} co-doped samples, with a specific focus on elucidating the energy transfer mechanism and temperature-dependent emission behaviors. Furthermore, the potential of these GCs for high-precision optical thermometry is evaluated by analyzing the fluorescence intensity ratio (FIR) of the Dy^{3+} and Eu^{3+} emissions as a function of temperature.

2. Experimental：

High-purity SiO_2, H_3BO_3, K_2CO_3, GdF_3, KF, Dy_2O_3, and EuF_3 powders (99% purity) were used as raw materials. Undoped, Dy^{3+}-doped, Eu^{3+}-doped, and Dy^{3+}/Eu^{3+}-co-doped KGd_2F_7 nanocrystalline glass-ceramics (GCs) were prepared by the conventional melt-quenching method. The precursor glasses (PGs) were synthesized according to the composition $65SiO_2$-$12H_3BO_3$-$15K_2CO_3$-(10-y)GdF_3-10KF-xDy_2O_3-yEuF_3, where x and y correspond to the molar doping concentrations of Dy_2O_3 and EuF_3, respectively, as listed in Table 1. For the co-doped samples, the Dy^{3+} concentration was fixed at 0.4 mol%, while the Eu^{3+} concentration was varied from 0 to 1.2 mol%(0, 0.3, 0.5, 0.8, 1.2 mol%).

The raw materials were accurately weighed according to the stoichiometric ratios, with a total batch mass of 40 g. The powders were thoroughly ground and mixed in an agate mortar to ensure compositional uniformity. The mixture was then transferred to a corundum crucible and melted at 1570 °C for 30 min in an electric furnace to obtain

a homogeneous melt. Subsequently, the melt was rapidly poured onto a pre-cooled metal plate to form a transparent precursor glass, thereby suppressing nucleation and crystallization.

The quenched precursor glass was subsequently annealed at 450 °C for 4 h. As reported in earlier studies, this thermal treatment effectively relieves residual stress in similar glass systems, thereby enhancing mechanical stability and preventing cracking[15, 16]. After annealing, the glass samples were cut, ground and polished into 10 × 10 × 1 mm^3 specimens for subsequent optical characterizations, including photoluminescence (PL) spectra, fluorescence lifetime measurements, and temperature-dependent emission measurements[17].

Table. 1 The molar composition of the precursor glasses (PGs)

Raw material(mol%): **65SiO_2-12H_3BO_3-15K_2CO_3-(10-y)GdF_3-10KF-xDy_2O_3-yEuF_3**						
GCs(name)	S1	S2	S3	S4	S5	S6
x	0	0.2	0.2	0.2	0.2	0.2
y	0.3	0	0.3	0.5	0.8	1.2

3. Results and discussion：

3.1. XRD and structure analysis

X-ray diffraction (XRD) analysis was conducted to elucidate the phase evolution and structural characteristics of the synthesized samples. Fig. 1(a) compares the XRD patterns of the precursor glass (PG), singly doped GCs, and co-doped GCs with the standard reference pattern of KGd_2F_7 (PDF#00-027-0387)[18-20]. Interestingly, distinct diffraction peaks attributed to the KGd_2F_7 crystal phase are identifiable even in the PG sample, revealing the intrinsic self-crystallizing behavior of the precursor matrix during the melt-quenching process. Additionally, a broad diffuse scattering background spanning 20° to 30° is persistently observed across all patterns, representing the characteristic halo signature of an amorphous phase[21, 22]. This confirms the coexistence of short-range atomic order (glass matrix) and long-range

structural periodicity (nanocrystals).

Upon the introduction of Dy^{3+} and Eu^{3+} dopants, the macroscopic monoclinic crystal framework—belonging to the I2/m space group (No. 12)—is well preserved. However, local structural modifications do occur. Specifically, the characteristic diffraction peak at $2\theta \approx 26.5°$ exhibits a noticeable reduction in intensity accompanied by slight peak broadening (Fig. 1(a)). To uncover the underlying mechanism, the relative effective ionic radius difference (Δr) was evaluated using the following formula[23]:

$$\Delta r = \frac{R_m(CN) - R_d(CN)}{R_m(CN)} \times 100\% \quad (1)$$

where CN is the coordination number, and R_m and R_d denote the ionic radii of the host (Gd^{3+}) and dopant ions, respectively. For sixfold coordination (CN = 6), the ionic radii are $r(Gd^{3+})$ = 1.053 Å, $r(Dy^{3+})$ = 1.027 Å, and $r(Eu^{3+})$ = 1.066 Å. The calculated radius mismatch is 2.47% for Dy^{3+} substitution, leading to local lattice contraction, and 1.26% for Eu^{3+} substitution, resulting in slight lattice expansion. Since both Δr values are well below the commonly accepted 15% size-mismatch criterion, substitution of Gd^{3+} by Dy^{3+}/Eu^{3+} ions is favorable for solid-solution formation. In the co-doped samples, the competing effects of lattice contraction and expansion generate a complex local distortion field, slightly perturbing the ideal Bragg diffraction conditions and thereby causing the observed peak broadening.

To quantitatively determine the structural parameters of the crystallized nanocrystals, whole-pattern fitting (WPF) was performed on the experimental XRD data, yielding unit cell parameters of a = 12.343 Å, b = 8.067 Å, c = 12.128 Å, β = 109.091°, and a cellular volume of V = 1141.3 $Å^3$ (Z = 8). The refinement gave R_{wp} = 10.75% and χ^2 = 1.8. The relatively high R_{wp} value is mainly attributed to the strong diffuse-scattering background from the residual amorphous glass matrix, which is an inherent feature of glass-ceramic systems. These refined parameters indicate that, aside from minor atomic displacement induced by local strain, the periodic lattice remains largely intact. Furthermore, based on the crystallographic model, the structure

is shown in Fig. 1(b), clearly revealing mixed occupancy of K^+ and Gd^{3+} at cation sites, along with partial occupancy of F^- sites. Such crystallographic features can facilitate charge compensation and reduce lattice energy, thereby improving structural stability when multiple rare-earth ions are uniformly incorporated for tunable photoluminescence applications[24-26].

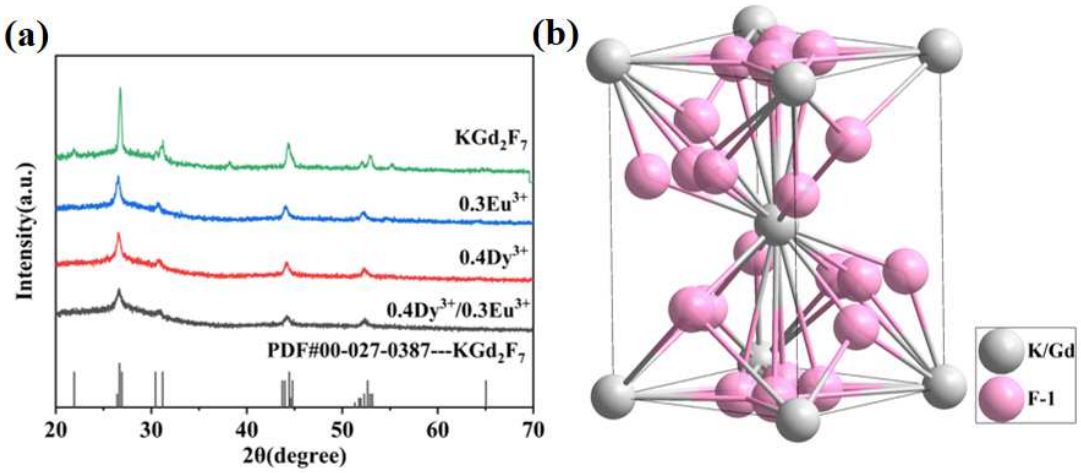


Fig. 1. (a) XRD patterns of undoped KGd_2F_7 GCs, singly doped with Dy^{3+}, Eu^{3+} and co-doped with Dy^{3+}/Eu^{3+}. (b) Ball-and-stick model of the crystal structure of the KGd_2F_7.

3.2. TEM Analysis

TEM and HRTEM were employed to examine the microstructure and crystallization behavior of the synthesized samples. As shown in Fig. 2(a) for Sample 6, quasi-spherical nanocrystals are homogeneously dispersed within the amorphous matrix, demonstrating the typical microstructural characteristics of GCs[27]. The selected-area electron diffraction (SAED) pattern in the inset of Fig. 2(a) shows a series of concentric diffraction rings, confirming the polycrystalline nature of the precipitated KGd_2F_7 phase[28].

Further microstructural details are revealed by the HRTEM image in Fig. 2(b), which displays well-ordered lattice fringes. The measured interplanar spacing is approximately 0.203 nm, in good agreement with the (323) crystallographic plane of monoclinic KGd_2F_7 (theoretical value: ~0.204 nm), further confirming the XRD results[29].

Energy-dispersive X-ray spectroscopy (EDX) was performed to determine the elemental composition of the examined region. The corresponding spectrum in Fig. 2(c) shows the characteristic signals of K, Gd, F, Dy, and Eu, while the prominent Si and O peaks originate from the silica-based glass network. The simultaneous detection of Dy and Eu confirms the successful incorporation of the rare-earth dopants into the glass-ceramic system.

Furthermore, statistical analysis of more than 50 individual particles (Fig. 2(d)) reveals a narrow size distribution ranging from 10 to 20 nm, with an average crystallite size of ~15.7 nm. Since this size is much smaller than the wavelength of visible light (400–700 nm), light scattering at the crystal–glass interfaces is effectively minimized. Consequently, this uniform nanoscale precipitation not only ensures the high transparency of the bulk GCs but also provides a low-phonon-energy crystalline environment favorable for the luminescence of the incorporated rare-earth ions[30].

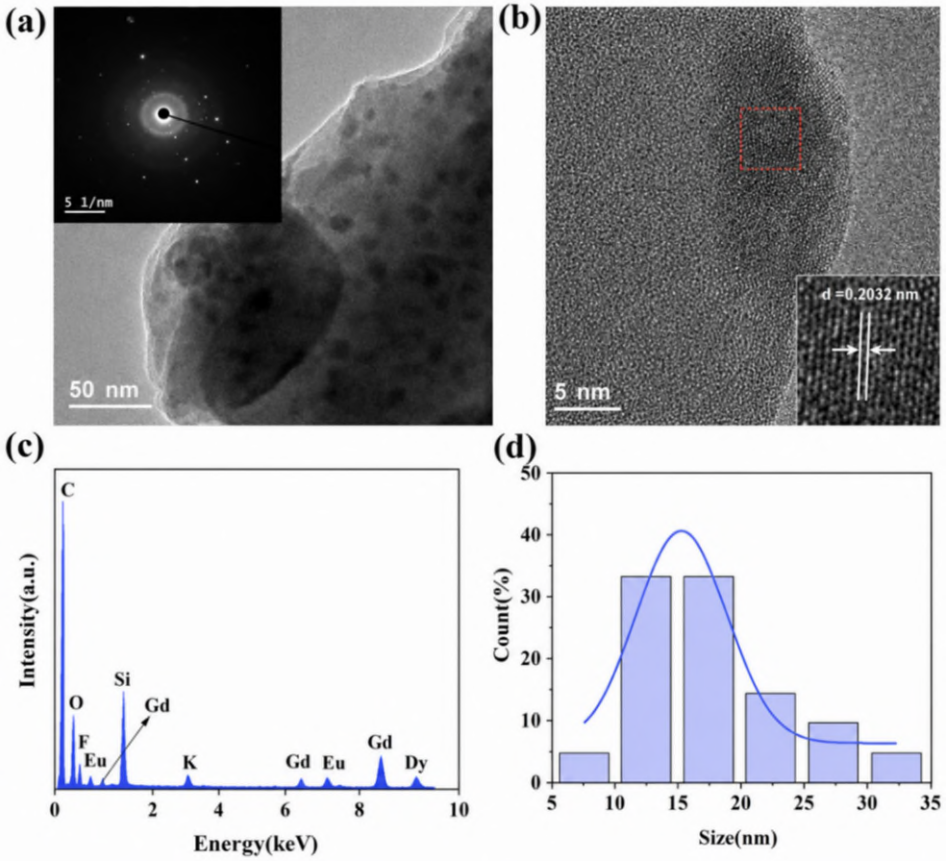


Fig. 2. (a) TEM image and corresponding SAED pattern. (b) HRTEM image. (c) EDX spectrum of the crystalline region. (d) Particle size distribution diagram.

3.3. Photoluminescence Properties and Site Symmetry Probing

To systematically evaluate the phoVtoluminescence (PL) performance of Dy^{3+} and Eu^{3+} doped KGd_2F_7 GCs, steady-state excitation and emission spectra were recorded. These optical signatures not only delineate the characteristic 4f–4f transitions of the lanthanide ions but also act as highly sensitive structural probes, providing crucial insights into the local coordination environment and crystal-field splitting, thereby laying a theoretical foundation for their application in photonic devices.

Monitored at the prominent 575 nm yellow emission, the photoluminescence excitation (PLE) spectrum of Dy^{3+} (Fig. 3(a)) exhibits multiple absorption bands spanning the 300–400 nm region. The discernible peaks at 325, 355, and 390 nm are accurately assigned to the transitions from the ground state $^6H_{15/2}$ to the excited states $^6P_{3/2,}$ $^6P_{7/2}$, and $^4I_{13/2}$, respectively[31]. The absolute dominance of the 355 nm excitation peak highlights the material's remarkable near-ultraviolet (n-UV) harvesting capability, perfectly bridging the excitation requirements of commercial n-UV LED chips for solid-state lighting.

Upon 355 nm excitation, the PL emission spectrum of Dy^{3+} (Fig. 3(b)) comprises two well-resolved bands centered at 488 nm (blue) and 580 nm (yellow), originating from the $^4F_{9/2}\rightarrow{}^6H_{15/2}$ and $^6H_{13/2}$, transitions, respectively[32]. Notably, the yellow emission (580 nm) exhibits an intensity approximately three times that of its blue counterpart (488 nm). According to Judd-Ofelt theory, the hypersensitive forced electric-dipole transition ($\Delta J = 2$, $^4F_{9/2}\rightarrow{}^6H_{13/2}$) is dominant only when the Dy^{3+} ions occupy crystallographic sites lacking inversion symmetry. This high Yellow-to-Blue (Y/B) ratio strictly confirms the low-symmetry crystal-field environment induced by the aforementioned lattice distortions.

For the Eu^{3+}-doped samples, the PLE spectrum monitored at 614 nm (Fig. 3(c)) reveals intense absorption features. Aside from the intra-configurational $^4f_6$–$^4f_6$ transitions at 320, 395, and 464 nm, a distinct band is observed around 280 nm, which can be primarily ascribed to the typical $^8S_{7/2}\rightarrow{}^6I_J$ transition of the host Gd^{3+} ions,

demonstrating an efficient $Gd^{3+}\rightarrow Eu^{3+}$ energy transfer channel[33]. The strongest peak at 395 nm ($^7F_0\rightarrow{}^5L_6$) further emphasizes the strong energy coupling with n-UV irradiation.

The corresponding PL emission spectrum under 395 nm excitation (Fig. 3(d)) exhibits four characteristic peaks at 557, 595, 616, and 704 nm, assigned to the $^5D_1\rightarrow{}^7F_0$ and $^5D_0\rightarrow{}^7F_J$ (J = 1, 2, 4) transitions, respectively[33]. Strikingly, the red emission at 616 nm, governed by the forced electric-dipole $^5D_0\rightarrow{}^7F_2$ transition, overwhelmingly dominates the spectrum compared to the magnetic-dipole $^5D_0\rightarrow{}^7F_1$ transition at 595 nm. This exceptionally high asymmetry ratio strictly corroborates the theoretical prediction that the Eu^{3+} activators reside in non-centrosymmetric local environments, which selectively relaxes the parity selection rules and enhances the red luminescence. These compelling spectroscopic traits establish the Eu^{3+}-doped KGd_2F_7 architecture as an ultra-efficient red-emitting candidate for advanced display and lighting technologies.

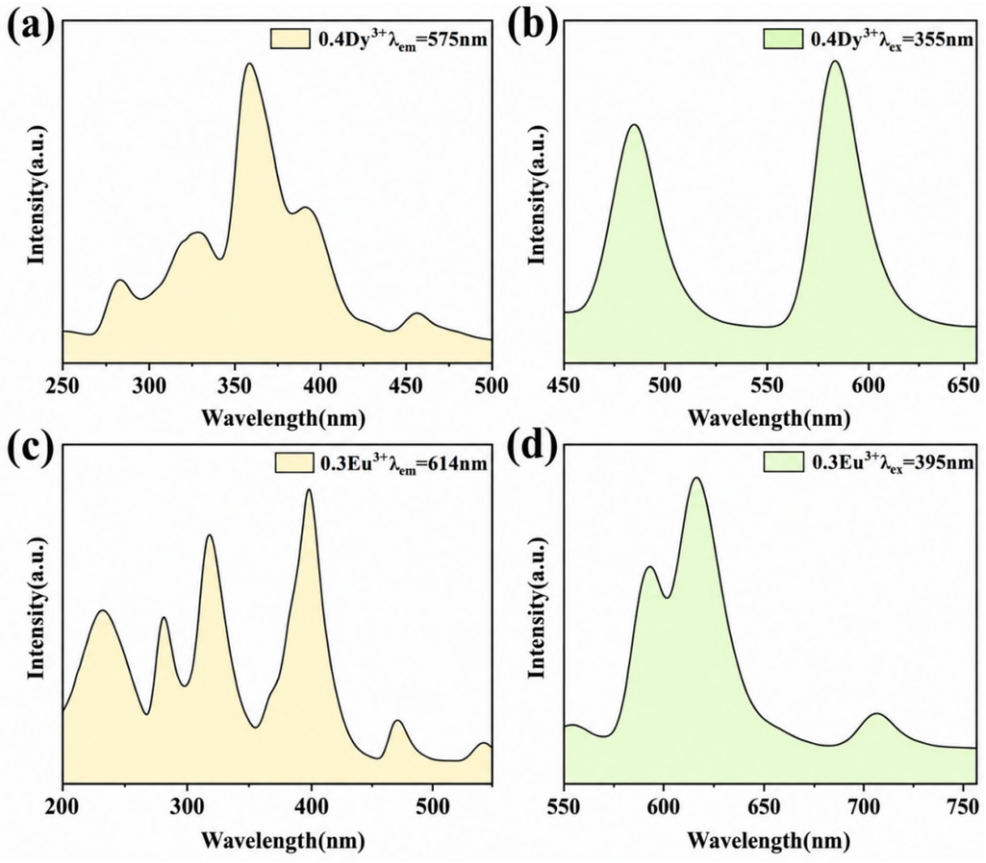


Fig. 3. (a) Excitation spectrum of 0.4 mol% Dy^{3+}. (b) Emission spectrum of 0.4 mol% Dy^{3+}. (c) Excitation spectrum of 0.3 mol% Eu^{3+}. (d) Emission spectrum of 0.3 mol% Eu^{3+}.

3.4. Emission Evolution and Color Tunability in Co-doped Systems

Fig. 4(a) illustrates the photoluminescence emission spectra of Dy^{3+}/Eu^{3+} co-doped GCs under 360 nm excitation. Distinct emission peaks are observed at 488 nm ($^4F_{9/2}\rightarrow{}^6H_{15/2}$) and 580 nm ($^4F_{9/2}\rightarrow{}^6H_{13/2}$), attributed to Dy^{3+} transitions, alongside a sharp red emission peak at 616 nm ($^5D_0\rightarrow{}^7F_2$) corresponding to Eu^{3+}. As shown in Fig. 4(b), the emission color progressively shifts from yellow to orange-red with increasing Eu^{3+} doping concentration. This demonstrates effective color tunability achieved by precisely adjusting the dopant ratio, offering critical functionality for photonic devices requiring customizable emission properties.

Fig. 4(c) presents the evolution of emission intensities at 580 nm (Dy^{3+}) and 616 nm (Eu^{3+}) as a function of Eu^{3+} content. As the Eu^{3+} concentration increases from 0 to 1.2 mol%, the yellow luminescence intensity at 580 nm steadily declines, while the red emission intensity at 616 nm rises sharply, peaking at 1.2 mol%. This inverse trend confirms an efficient energy transfer (ET) process from Dy^{3+} ions (sensitizer) to Eu^{3+} ions (activator). The ET mechanism effectively populates the excited states of $Eu3^+$, thereby enhancing red emission while simultaneously reducing the luminescence intensity of Dy^{3+}[34].

To quantify this interaction, Fig. 4(d) displays the normalized emission intensities. With increasing Eu^{3+} concentration from 0 to 1.2 mol%, the Dy^{3+} emission decreases from 1.00 to 0.60, whereas the Eu^{3+} emission surges from 0.06 to 1.00. Remarkably, no concentration quenching of Eu^{3+} luminescence is observed within the studied doping range. This highlights the high stability of activator ions within the KGd_2F_7 host lattice, a feature particularly advantageous for achieving efficient optical outputs in high-doping systems.

$$CP=\frac{\sqrt{(x-x_z)^2+\left(y-y_z\right)^2}}{\sqrt{(x_a-x_z)^2+\left(y_a-y_z\right)^2}}\times 100\% \quad (2)$$

The chromaticity coordinates of the samples are shown in Fig. 5, with error bars representing measurement uncertainties. The color purity was calculated using Equation (2)[35], wherein x_z and y_z represent the coordinates of pure white light

(0.3333, 0.3333); x_a and y_a correspond to the dominant wavelength, while x and y indicate the CIE coordinates of specimens with varying doping levels. As summarized in Table 1, the color purity exhibits a linear increase with increasing Eu^{3+} doping concentrations, rising from 0.58 at 0.3 mol% to 0.82 at 1.2 mol%. This analysis confirms a significant improvement in spectral purity, directly attributable to elevated activator concentrations.

Finally, Figs. 6(a–d) provides visual confirmation of these spectral changes, showing photographs of the physical samples under UV excitation. The luminescent color visibly transitions from near-white/yellowish to high-purity orange and deep red. Collectively, these findings confirm that the emission color can be finely tuned by adjusting the Dy^{3+}/Eu^{3+} ratio, offering customizable luminescent properties suitable for advanced applications such as high-efficiency red LEDs, multicolor displays, and bioimaging systems.While the tunable macroscopic luminescence and the inverse trends in steady-state emission intensities strongly imply an underlying energy transfer process from Dy^{3+} to Eu^{3+}, a rigorous quantitative analysis of the luminescence dynamics is required to fully elucidate this mechanism.

Table. 2 CIE coordinates and color purity (CP) values of the samples with different doping concentrations.

No.	Composition(mol%)	CIE(x,y)	(x_a,y_a)	CP(%)
S2	$0.4Dy^{3+}$	(0.4104,0.4171)	(0.4745,0.5251)	57.87
S3	$0.4Dy^{3+}/0.3Eu^{3+}$	(0.4489,0.4073)	(0.5003,0.4963)	62.23
S4	$0.4Dy^{3+}/0.5Eu^{3+}$	(0.4704,0.4016)	(0.5129,0.4812)	67.58
S5	$0.4Dy^{3+}/0.8Eu^{3+}$	(0.4925,0.3900)	(0.5298,0.4610)	73.79
S6	$0.4Dy^{3+}/1.2Eu^{3+}$	(0.5211,0.3836)	(0.5521,0.4372)	81.95

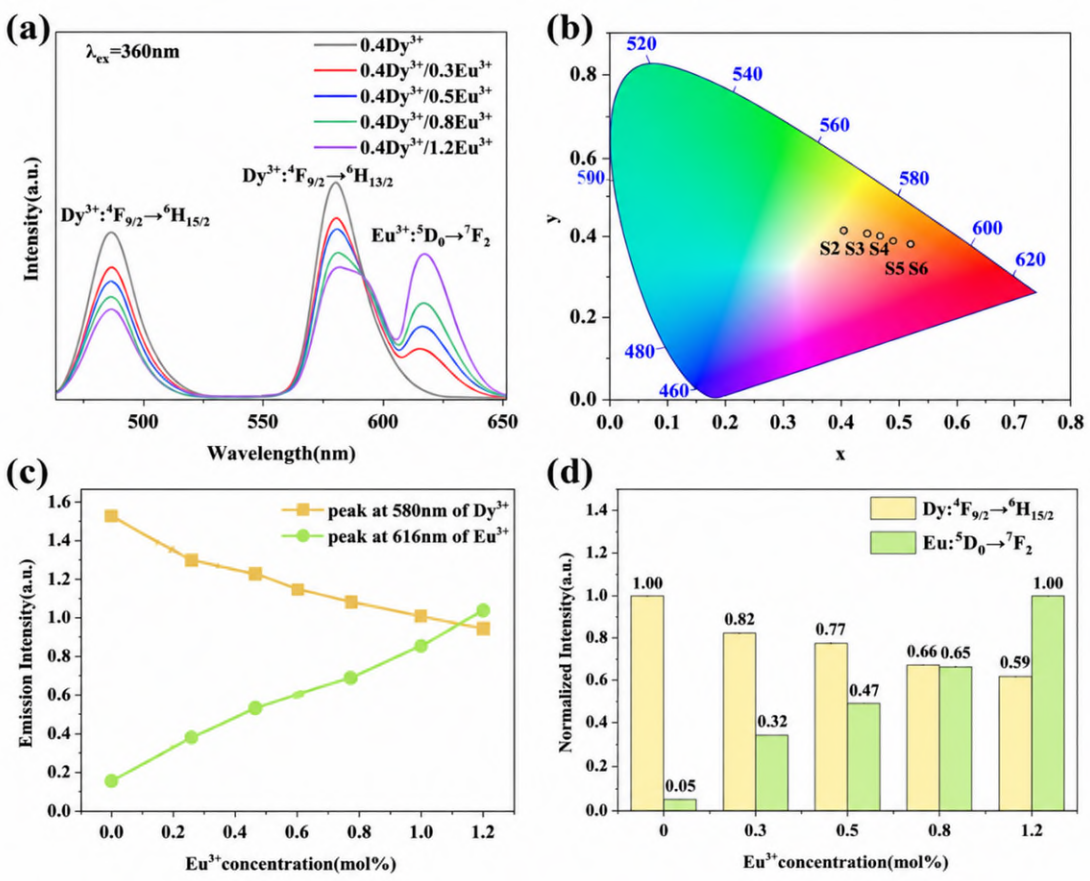


Fig. 4. (a) Photoluminescence emission spectra of KGd_2F_7 co-doped with Dy^{3+}/Eu^{3+} at varying Eu^{3+} concentrations under 360 nm excitation. (b) CIE chromaticity coordinates of KGd_2F_7 glass-ceramics doped with 0.4 mol% Dy^{3+}/yEu^{3+} (y = 0, 0.3, 0.5, 0.8, 1.2 mol%). (c) Emission intensity of Dy^{3+} and Eu^{3+} as a function of Eu^{3+} concentration. (d) Normalized emission intensity of Dy^{3+} and Eu^{3+} as a function of Eu^{3+} concentration.

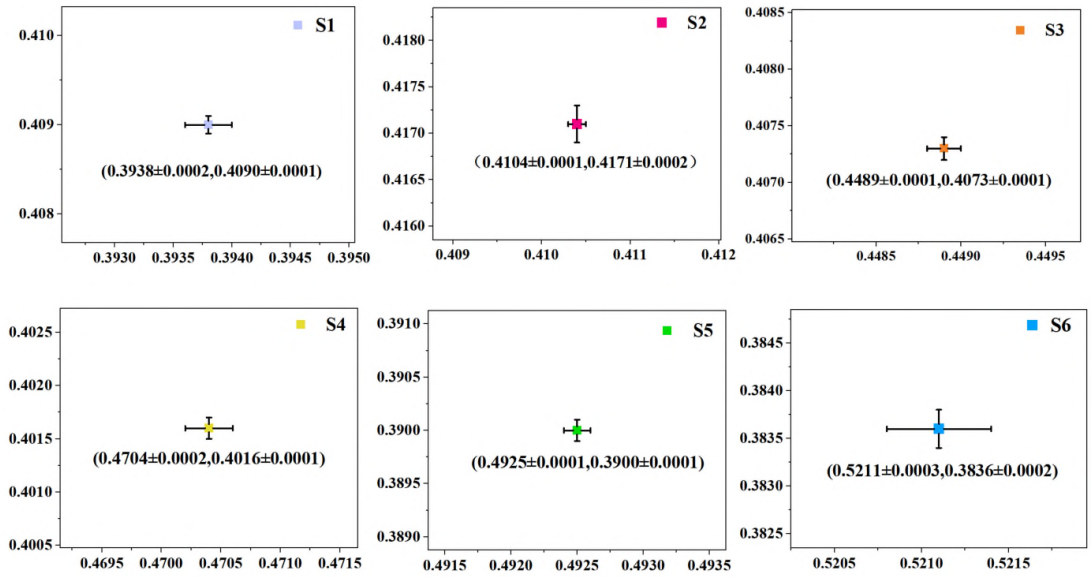


Fig. 5. CIE chromaticity coordinates with error bars for samples S1–S6

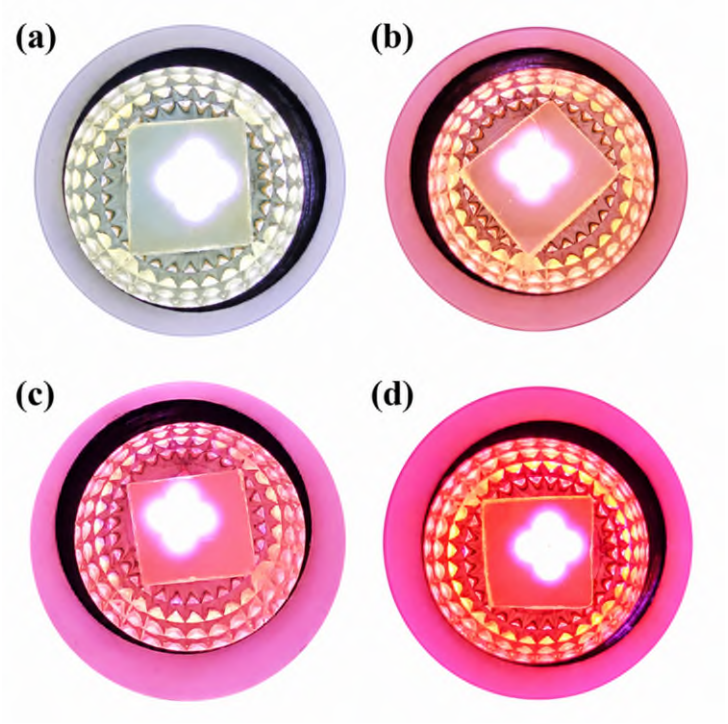


Fig. 6. (a-d) Physical luminescence color photographs of KGd_2F_7 GCs samples doped with 0.4 mol% Dy^{3+}/yEu^{3+} (y = 0, 0.3, 0.8, 1.2 mol%).

3.5. Luminescence Dynamics and Energy Transfer Mechanism

Fig. 7(a) shows the energy level diagram and energy transfer (ET) pathways of Dy^{3+} and Eu^{3+} in the KGd_2F_7 glass system. Under 360 nm excitation, Dy^{3+} absorbs incident photons and electrons are excited from the ground state to the excited $^6P_{7/2}$ level[36]. These electrons then relax non-radiatively (NR) to the lower $^4F_{9/2}$ state, and subsequently return to the ^6H_J ground state manifolds via radiative decay. This process produces characteristic blue emission at 488 nm ($^4F_{9/2}\rightarrow{}^6H_{15/2}$) and yellow emission at 580 nm ($^4F_{9/2}\rightarrow{}^6H_{13/2}$)[37].

Meanwhile, part of the excitation energy at the Dy^{3+} $^4F_{9/2}$ state transfers to adjacent Eu^{3+} through resonant energy transfer. As a result, Eu^{3+} is excited to the $^5L_6$ level and relaxes non-radiatively to the metastable $^5D_0$ state. Radiative transitions from $^5D_0$ to ^7F_J (J = 0, 1, 2) generate typical red emission. This energy transfer behavior explains the quenched Dy^{3+} luminescence and enhanced Eu^{3+} emission observed in steady-state spectra. As presented in Fig. 7(b), the significant spectral overlap between Dy^{3+} emission bands ($^4F_{9/2}\rightarrow{}^6H_J$) and Eu^{3+} excitation bands satisfies

the resonance condition required for efficient $Dy^{3+}\rightarrow Eu^{3+}$ energy transfer.

Fluorescence decay characteristics of KGd_2F_7:0.4 mol% Dy^{3+}/y Eu^{3+} (y = 0, 0.3, 0.5, 0.8, 1.2 mol%) were measured to quantitatively verify the energy transfer mechanism. As shown in Fig. 8(a), all decay curves are well fitted by a double-exponential function:

$$I_t=A_1\exp\left(-\frac{t}{\tau_1}\right)+A_2\exp\left(-\frac{t}{\tau_2}\right)+I_0 \quad (3)$$

where I(t) is the luminescence intensity at time t, τ_1 and τ_2 are fast and slow decay components, and A_1 and A_2 are fitting constants[33]. The average lifetime (τ) is calculated using the formula below:

$$\tau=(A_1\tau_1^2+A_2\tau_2^2)/(A_1\tau_1+A_2\tau_2) \quad (4)$$

The average emission lifetimes of Dy^{3+} are 320.57 ns, 248.83 ns, 188.54 ns, 142.35 ns and 104.51 ns when Eu^{3+} concentrations are 0, 0.3, 0.5, 0.8 and 1.2 mol%. The steady decrease of Dy^{3+} lifetime with increasing Eu^{3+} concentration strongly confirms the existence of energy transfer.Energy transfer efficiency (η_{ET}) is calculated as follows[38]:

$$\eta_{ET}=1-\frac{\tau_S}{\tau_{So}} \quad (5)$$

where τ_S and τ_{S0} stand for Dy^{3+} lifetimes in co-doped and single-doped samples, respectively. Fig. 8(b) reveals that η_{ET} rises steadily with Eu^{3+} content, reaching 0%, 20.8%, 31.8%, 43.5% and 55.6% at corresponding doping levels.

Dexter's theory was adopted to determine the multipolar interaction type of energy transfer, with the relational expression shown below:

$$\frac{I_{Dy}}{I_{Dy\text{-}Eu}}\propto\frac{\tau_{Dy}}{\tau_{Dy\text{-}Eu}}\propto C^{\frac{n}{3}} \quad (6)$$

In this formula, C is the total doping concentration. The value of n distinguishes interaction types: n = 6 for dipole–dipole interaction, n = 8 for dipole–quadrupole interaction, and n = 10 for quadrupole–quadrupole interaction. According to the linear fitting results in Fig. 9, the correlation coefficient reaches the maximum when n = 10. It proves that quadrupole–quadrupole interaction dominates the $Dy^{3+}\rightarrow Eu^{3+}$ energy transfer in the KGd_2F_7 host.

With high energy transfer efficiency and controllable luminescence performance, the KGd_2F_7 glass-ceramic is a promising material for multicolor emission in advanced photonic devices.

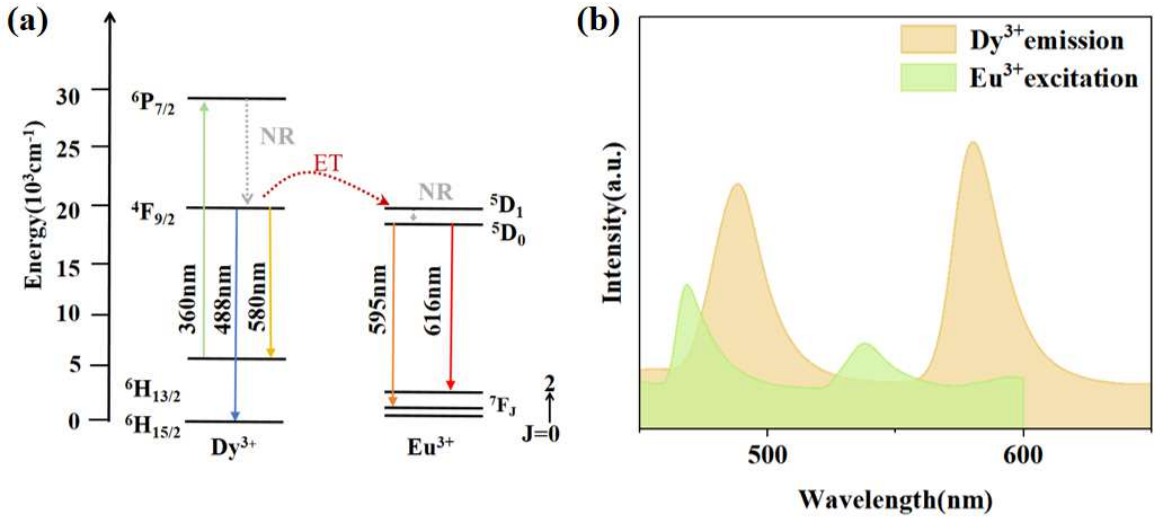


Fig. 7. (a) Energy level transition schematic of Dy^{3+}/Eu^{3+} co-doped system. (b) Emission (Dy^{3+}) and excitation (Eu^{3+}) spectra of singly doped samples.

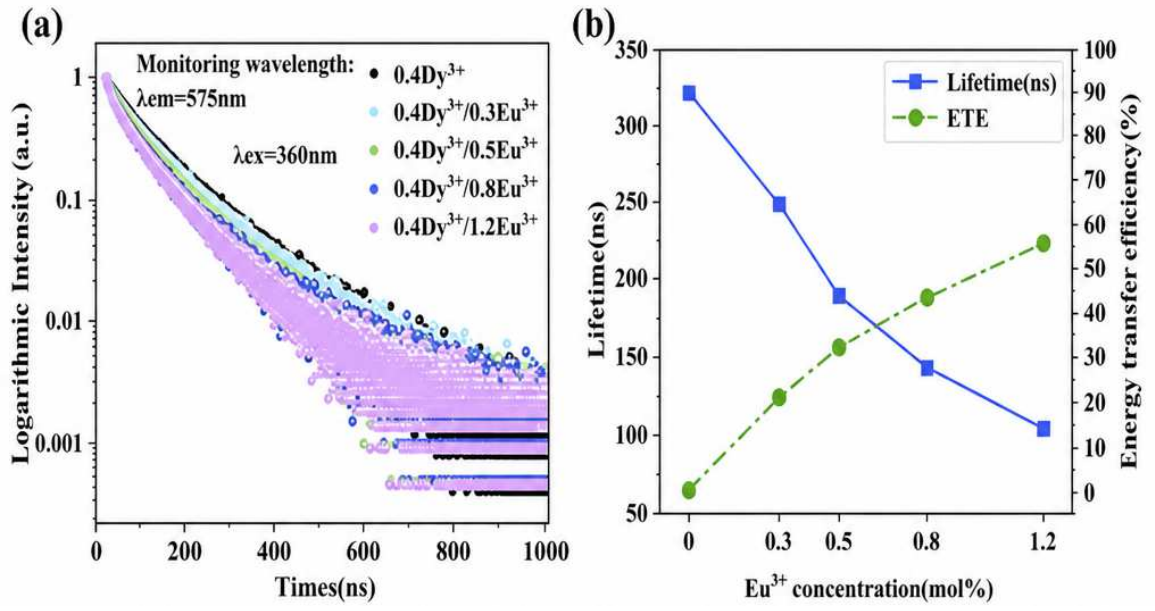


Fig. 8. (a) Fluorescence lifetime of Dy^{3+} in KGd_2F_7: 0.4 mol% Dy^{3+}/ yEu^{3+} (y=0, 0.3, 0.5, 0.8, 1.2 mol%) samples. (b) Relationship between fluorescence lifetime, ET efficiency and Eu^{3+} concentration.

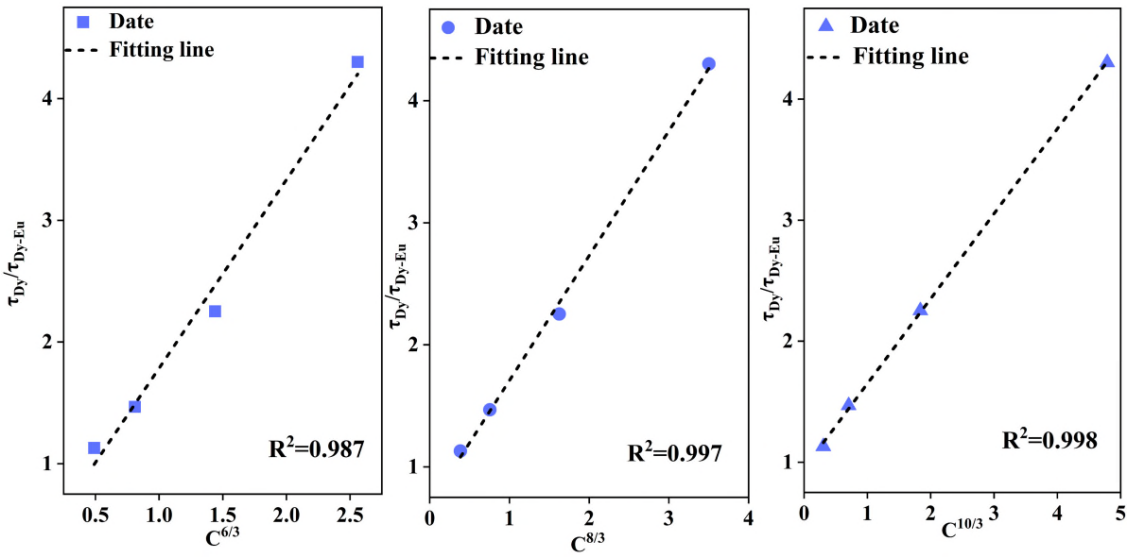


Fig. 9. Linear fitting of $\tau_{Dy}/\tau_{Dy\text{-}Eu}$ against $C^{6/3}$, $C^{8/3}$, and $C^{10/3}$.

3.6. Temperature Sensing Properties Based on Fluorescence Intensity Ratio

The temperature-dependent luminescence behavior and optical thermometric performance of the as-synthesized samples were systematically investigated using temperature-dependent emission spectra and luminescence decay measurements.

Figs. 10(a) and 10(b) show the emission spectra and normalized intensities of the KGd_2F_7 glass-ceramic co-doped with 0.4 mol% Dy^{3+} and 1.2 mol% Eu^{3+} over a temperature range of 298–548 K. With increasing temperature, the normalized emission intensities of both the Dy^{3+} ($^4F_{9/2}\rightarrow{}^6H_{13/2}$) and Eu^{3+} ($^5D_0\rightarrow{}^7F_2$) bands gradually decrease. This behavior is mainly attributed to enhanced lattice vibrations at elevated temperatures, which increase the probability of non-radiative relaxation and consequently lead to thermal quenching. Notably, the Dy^{3+} emission decreases more rapidly than the Eu^{3+} emission, indicating that the Dy^{3+} center is more sensitive to temperature changes. In contrast, the Eu^{3+} center exhibits better thermal stability, resulting in a slower intensity decay. The different thermal quenching behaviors of the Dy^{3+} and Eu^{3+} emission bands demonstrate distinct temperature responses of the two luminescent centers, providing the basis for fluorescence intensity ratio (FIR)-based optical thermometry.

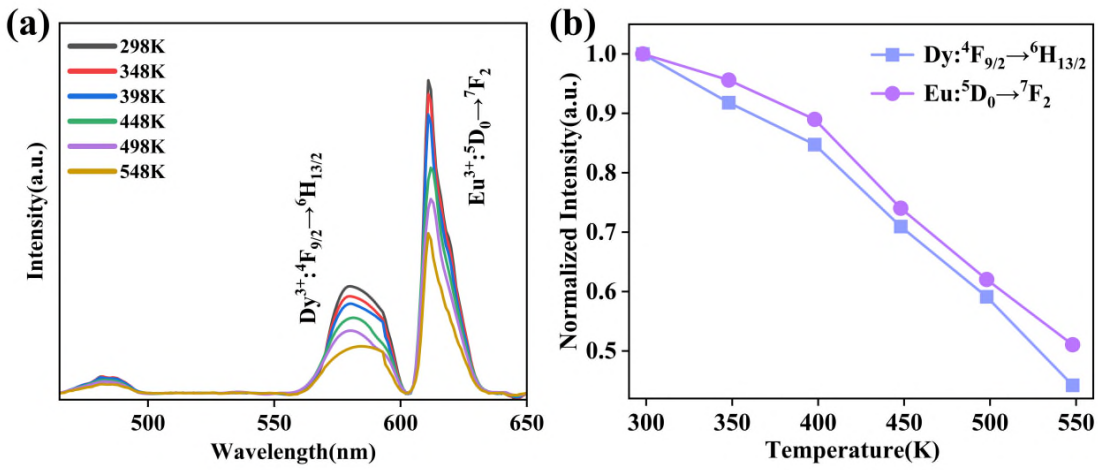


Fig. 10. (a) Temperature-dependent emission spectra of S6. (b) The normalized intensity of $Dy^{3+}$and $Eu^{3+}$with the rise of temperature.

The performance of optical temperature sensors is commonly evaluated in terms of absolute sensitivity and relative sensitivity. Fig. 11(a) presents the experimental data and fitting curve of the fluorescence intensity ratio (FIR = I_{Dy}/I_{Eu}) as a function of temperature for the sample co-doped with 0.4 mol% Dy^{3+} and 1.2 mol% Eu^{3+}. With increasing temperature, the FIR corresponding to the characteristic emission bands of Dy^{3+} and Eu^{3+} decreases monotonically, indicating a clear negative correlation. This result suggests that the present system has good temperature responsiveness and holds promise for optical temperature sensing applications.

The relationship between temperature and the fluorescence intensity ratio can be expressed as follows[39]:

$$FIR = C \exp(\frac{-\Delta E}{kT}) \quad (7)$$

where C is a constant, ΔE denotes the thermal activation energy associated with co-doped Dy^{3+} and Eu^{3+} ions in the KGd_2F_7 glass-ceramic, and k and T denote the Boltzmann constant and absolute temperature, respectively. The absolute sensitivity (S_a) and relative sensitivity (S_r) can be calculated using the following equations[40]:

$$S_a = \left|\frac{\partial FIR}{\partial T}\right| \quad (8)$$

$$S_r = \left|\frac{1}{FIR}\frac{\partial FIR}{\partial T}\right| \quad (9)$$

Figs. 11(b) and 11(c) display the temperature-dependent curves of absolute sensitivity (S_a) and relative sensitivity (S_r) for the sample within the test range of 298–

548 K. As shown in these figures, both S_a and S_r decrease monotonically with increasing temperature, and their peak values are achieved at 298 K. The maximum absolute sensitivity S_a is 0.372 $\%K^{-1}$, while the peak relative sensitivity S_r reaches 0.388 $\%K^{-1}$. To comprehensively evaluate the thermometric performance of this glass-ceramic, Table 3 presents a comparison of the sensitivity parameters of the present system with those of classical luminescent thermometric materials reported in previous literature. The comparison indicates that the sensitivity indicators of the sample in this work are superior to those of most reported optical temperature sensors based on the fluorescence intensity ratio (FIR) strategy.

Temperature resolution refers to the minimum detectable temperature variation under a given precise measurement condition, which can be calculated according to the following formula[41]:

$$\delta T = \frac{1}{S_r} \frac{\partial FIR}{FIR} \tag{10}$$

In this equation, $\frac{\partial FIR}{FIR}$ denotes the relative experimental error during measurement, which is limited by the performance of the testing equipment. The signal-to-noise ratio (SNR) of the fluorescence spectrometer used in this work is 25000:1, corresponding to $\frac{\partial FIR}{FIR}$ value of approximately 0.008%. Fig. 11(d) presents the temperature resolution of the KGd_2F_7 glass-ceramic co-doped with 0.4 mol% Dy^{3+} and 1.2 mol% Eu^{3+} over the temperature range of 298–548 K. Throughout the entire measurement range, the temperature resolution remains at a relatively low level, varying from 0.021 K to 0.069 K. Such a low temperature resolution enables the detection of minute temperature variations, indicating its potential for high-precision thermometry at low temperatures, such as in biological sensing and environmental monitoring. Moreover, the temperature resolution increases gradually and monotonically with temperature, without abrupt fluctuations, suggesting stable thermometric behavior and excellent measurement reproducibility. Overall, this material exhibits high sensitivity over a wide temperature range and favorable physicochemical properties, demonstrating promising potential for precise wide-range optical thermometry.

Table. 3. Optical thermometric performances of several typical temperature-sensing materials.

Sensing materials	Temperature(K)	S_a(%K^{-1})	S_r(%K^{-1})	Rf
$SrLaGaO_4$: Dy^{3+}/Eu^{3+}	298—423	0.61	0.36	[42]
$Na_5Y_9F_{32}$: Ce^{3+}/Tb^{3+}	298—473	0.157	1.18	[43]
YBO_3: Ce^{3+}/Tb^{3+}	288—328	0.012	0.498	[44]
KY_3F_{10}:Tb^{3+}/Eu^{3+}	290—420	0.08	0.24	[45]
KGd_2F_7: Dy^{3+}/Eu^{3+}	298—548	0.372	0.388	This work

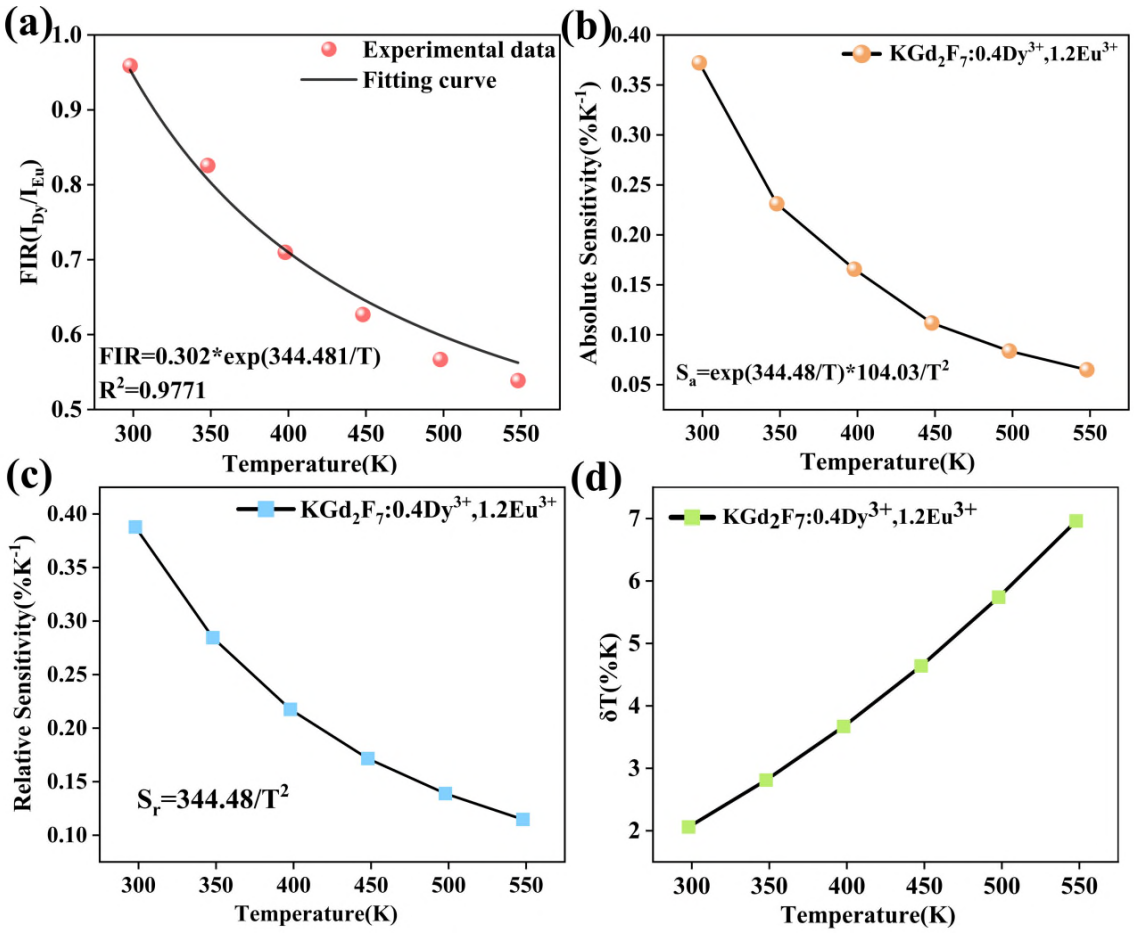


Fig. 11. (a) Dependence of FIR on temperature. (b) Absolute sensitivity. (c) Relative sensitivity. (d) Temperature resolution

Conclusion

In summary, Dy^{3+}/Eu^{3+}-co-doped KGd_2F_7 GCs were synthesized via a high-temperature melt-quenching method. Structural characterizations confirmed the uniform precipitation of well-crystallized KGd_2F_7 nanocrystals (average size ~15.7 nm) embedded within the glass matrix. Efficient energy transfer from Dy^{3+} to Eu^{3+} was realized in the GCs, enabling continuous emission color tuning from yellow to orange-red by varying the Eu^{3+} doping concentration, with the optimal Eu^{3+} emission intensity achieved at 1.2 mol%. Fluorescence lifetime analysis revealed a maximum energy transfer efficiency of 55.6%, and the dominant energy transfer mechanism was identified as quadrupole–quadrupole interaction on the basis of Dexter's theory.

Moreover, the optimal sample (0.4 mol% Dy^{3+}/1.2 mol% Eu^{3+}) exhibited outstanding thermometric performance over the temperature range of 298–548 K. It delivered a maximum absolute sensitivity (S_a) of 0.372 % K^{-1} and a relative sensitivity (S_r) of 0.388 % K^{-1}. In addition, the temperature resolution (δT) was as low as 0.021 K at room temperature, which verifies its ultrahigh temperature measurement precision.

In conclusion, the as-prepared materials act as promising candidates for high-performance lighting and multicolor display devices, and possess remarkable application potential in the field of optical temperature sensing. This work also offers valuable guidance for the design of self-crystallized oxyfluoride GCs with efficient rare-earth ion energy transfer and high-sensitivity thermometric capability.

References

[1] Jia, Y. et al. Integrated Photonics Based on Rare-Earth Ion-Doped Thin-Film Lithium Niobate. Laser & Photonics Reviews (2022).http://dx.doi.org/10.1002/lpor.202200059

[2] Okura, T., Nojima, Y., Kawada, K., Kojima, Y. & Yamashita, K. Photoluminescence properties of rare-earth ion-doped $Na_5YSi_4O_{12}$-based glass ceramics. Ceramics International (2021).http://dx.doi.org/10.1016/j.ceramint.2020.09.023

[3] Zheng, B. et al. Rare-Earth Doping in Nanostructured Inorganic Materials. Chemical Reviews (2022).http://dx.doi.org/10.1021/acs.chemrev.1c00644

[4] Xu, Z. et al. A new color-adjustable self-emitting in $SrGa_2Ge_2O_8$ substituted by Eu^{3+}, energy transfer and the determination of luminescence center. Journal of Luminescence (2020).http://dx.doi.org/10.1016/j.jlumin.2020.117194

[5] Kaçar, R., Serin, R.B., Uçar, E. & Ülkü, A. A review of high-end display technologies focusing on inkjet printed manufacturing. Materials Today Communications (2023).http://dx.doi.org/10.1016/j.mtcomm.2023.105534

[6] Xue, D., Teunter, R.H., Zhu, S.X. & Zhou, W. Entering the high-end market by collecting and remanufacturing a competitor's high-end cores. Omega (2019).http://dx.doi.org/10.1016/j.omega.2019.102168

[7] McFarland, B. & Opila, E. Investigations into the thermal stability of sol-gel-derived glasses as models for thermally grown oxides. Journal of the American Ceramic Society (2020).http://dx.doi.org/10.1111/jace.17314

[8] Wang, F. et al. Effect of cerium oxide on phase composition, structure, thermal stability and aqueous durability of sodium-iron-boron-phosphate based glasses. Journal of Nuclear Materials (2021).http://dx.doi.org/10.1016/j.jnucmat.2021.153199

[9] Tang, W. et al. Effect of introduction of TiO_2 and GeO_2 oxides on thermal stability and 2 μm luminescence properties of tellurite glasses. Ceramics International (2019).http://dx.doi.org/10.1016/j.ceramint.2019.05.171

[10] Grodecki, K. et al. Raman scattering of low energy HgCdTe phonons. Infrared Physics & Technology (2022).http://dx.doi.org/10.1016/j.infrared.2022.104318

[11] Kindrat, I.I. & Padlyak, B.V. Luminescence properties and quantum efficiency of the Eu-doped borate glasses. Optical Materials (2018).http://dx.doi.org/10.1016/j.optmat.2018.01.019

[12] Lin, H., Wen, T., Zhang, W., Gong, Q. & Lu, G. Chiral Luminescence Quantum Efficiency Engineered by Plasmonic Antennas. The Journal of Physical Chemistry C (2023).http://dx.doi.org/10.1021/acs.jpcc.2c08539

[13] Kim, K., Nam, S.K. & Moon, J.H. Dual-Band Luminescent Solar Converter-Coupled Dye-Sensitized Solar Cells for High-Performance Semitransparent Photovoltaic Device. ACS Applied Energy Materials (2020).http://dx.doi.org/10.1021/acsaem.0c00171

[14] Zhang, X. et al. Multi-talented luminescent hydroxyapatite nanocrystals toward high-performance fiber fabric and optoelectronic devices. Journal of Luminescence (2025).http://dx.doi.org/10.1016/j.jlumin.2025.121685

[15] National Commissioners on High Quality Health Systems, n. National Commissions on High Quality Health Systems: activities, challenges, and future directions. The Lancet Global Health (2019).http://dx.doi.org/10.1016/s2214-109x(18)30528-x

[16] Huong, T.T. et al. Functionalized $YVO_4:Eu^{3+}$ nanophosphors with desirable properties for

biomedical applications. Journal of Science: Advanced Materials and Devices (2016).http://dx.doi.org/10.1016/j.jsamd.2016.07.010

[17] Naik, P.S.R., Kumar, M.K., Babu, Y.N.C.R. & Kumar, A.S. Spectroscopic studies of Eu^{3+}: PbO–Bi_2O_3–WO_3–B_2O_3 glasses. Indian Journal of Physics(2013). http://dx.doi.org/10.1007/s12648-013-0284-6

[18] Li, W. et al. Crystal growth and visible fluorescence and energy transfer features of Dy^{3+}/RE^{3+} (RE=Tb,Eu)-codoped $Y_3Al_5O_{12}$ crystals. Journal of Luminescence (2022).http://dx.doi.org/10.1016/j.jlumin.2022.118864

[19] Wu, K. et al. High-Luminance Red $Ba_2CaB_2Si_4O_{14}$: Eu^{3+} with "Abnormal" Thermal Stability and Adjustable Photoluminescence from Defect Regulation and Energy Transfer via Dy^{3+} Codoping for "Warm" Illumination and Pressure Sensing Applications. Crystal Growth & Design (2025).http://dx.doi.org/10.1021/acs.cgd.5c00232

[20] Chen, W., Zhang, H. & Zhu, D. Preparation, optical properties and energy transfer of $SrLaAlO_4$: Dy^{3+}, Eu^{3+}. *Journal of Rare Earths* (2023).http://dx.doi.org/10.1016/j.jre.2023.11.001

[21] de Oliveira, A.S. et al. Photoluminescence, thermal stability and structural properties of Eu^{3+}, Dy^{3+} and Eu^{3+}/Dy^{3+} doped apatite-type silicates. Journal of Luminescence (2020).http://dx.doi.org/10.1016/j.jlumin.2020.117500

[22] Li, F., Liu, X. & He, T. Solid state synthesis of $CaTiO_3$:Dy^{3+}/Eu^{3+} phosphors towards white light emission. Chemical Physics Letters (2017).http://dx.doi.org/10.1016/j.cplett.2017.08.042

[23] Meza-Rocha, A.N., Speghini, A., Bettinelli, M. & Caldiño, U. White light generation through $Zn(PO_3)_2$ glass activated with Eu^{3+} and Dy^{3+}. Journal of Luminescence (2016).http://dx.doi.org/10.1016/j.jlumin.2016.03.035

[24] Shinde, V.V., Tiwari, A. & Dhoble, S.J. Synthesis of RE^{3+} (RE^{3+} = Ce^{3+}, Dy^{3+}, Eu^{3+} and Tb^{3+}) activated Gd_2SiO_5 optoelectronics materials for lighting. Journal of Molecular Structure (2020).http://dx.doi.org/10.1016/j.molstruc.2020.128397

[25] Zheng, Z. et al. Tb^{3+}-doped transparent $BaGdF_5$ glass-ceramics scintillator for X-ray detector. Journal of the American Ceramic Society (2019).http://dx.doi.org/10.1111/jace.16941

[26] Hu, M. et al. Influence of codoped Gd^{3+} ions on the spectroscopic site symmetry of Dy^{3+} ions in LaF_3 single crystals. Journal of Materials Chemistry C (2019).http://dx.doi.org/10.1039/c9tc02951f

[27] Dehghan-Niri, R. et al. Nanostructural Analysis of Co-Re/γ-Al_2O_3 Fischer-Tropsch Catalyst by TEM and XRD. ChemCatChem (2022).http://dx.doi.org/10.1002/cctc.202101931

[28] Ding, H., Cai, Y., Ren, K. & Zhang, Y. Optical properties and energy transfer of Bi^{3+}/Tb^{3+} doped $Ba_4Y_3F_{17}$ transparent glass-ceramics. Ceramics International (2026).http://dx.doi.org/10.1016/j.ceramint.2026.01.027

[29] Gao, Y. et al. Linear Scaling Relationships between Relative Diffraction Peak Intensity and Catalytic Oxidation of Light Alkanes. ACS Catalysis (2025).http://dx.doi.org/10.1021/acscatal.5c07646

[30] Wei, Y. et al. Structural evolution induced preferential occupancy of designated cation sites by Eu^{3+} in $M_5(Si_3O_9)_2$ (M = Sr, Ba, Y, Mn) phosphors. RSC Advances (2016).http://dx.doi.org/10.1039/c6ra11681g

[31] Zhang, B. et al. The comparison: photoluminescence and afterglow behavior in $CaSnO_3$:Dy^{3+} and Ca_2SnO_4:Dy^{3+} phosphors. Journal of Materials Science: Materials in Electronics (2017).http://dx.doi.org/10.1007/s10854-017-6964-9

[32] Sun, H. et al. Dy^{3+} and Gd^{3+} Complexes with Dy^{3+} Exhibiting Field-Induced Single-Molecule Magnet Behaviour. Journal of Molecular Structure (2022).http://dx.doi.org/10.1016/j.molstruc.2022.134111

[33] Thien, N.D., Vu, L.V. & Long, N.N. The effect of interaction between surface plasmons of gold nanoparticles and optical active centers on luminescence of Eu^{3+}-doped Zn_2SnO_4 nanocrystals. Optical Materials (2018).http://dx.doi.org/10.1016/j.optmat.2018.02.039

[34] Qi, Y. et al. Ce^{3+} sensitized Tb^{3+} and Dy^{3+} photoluminescence in β-LaB_5O_9 prepared by sol–gel method. Journal of Rare Earths (2021).http://dx.doi.org/10.1016/j.jre.2021.08.008

[35] Cai, Y., Ren, K., Ding, H. & Zhang, Y. Color tunability and thermal-enhanced luminescence of Ce^{3+}/Tb^{3+} Co-doped Ba_2LaF_7 glass ceramics. Journal of Alloys and Compounds (2025).http://dx.doi.org/10.1016/j.jallcom.2025.184453

[36] Mbule, P., Mlotswa, D., Mothudi, B. & Dhlamini, M. Photoluminescence and Thermoluminescence analysis of Zn_2SiO_4:Dy^{3+} nanophosphor. Journal of Luminescence (2021).http://dx.doi.org/10.1016/j.jlumin.2021.118060

[37] Ćirić, A., Stojadinović, S. & Dramićanin, M.D. Time-integrated luminescence thermometry of Eu^{3+} and Dy^{3+} doped YVO_4. Sensors and Actuators A: Physical (2019).http://dx.doi.org/10.1016/j.sna.2019.06.035

[38] Ren, K., Ke, L., Zou, Z., Zhao, E. & Zhang, Y. Optical properties, and thermal stability of Tb^{3+}/Pr^{3+}-doped $Na(Y_{1.5}Na_{0.5})F_6$ glass ceramics. Materials Characterization (2024).http://dx.doi.org/10.1016/j.matchar.2024.114655

[39] Hu, X. et al. Opposite temperature luminescent behaviours of Tb^{3+} and Pr^{3+} co-doped $BaMoO_4$ glass ceramics for temperature sensing. Journal of Luminescence (2021).http://dx.doi.org/10.1016/j.jlumin.2021.118080

[40] Zheng, Z. et al. Luminescence and self-referenced optical temperature sensing performance in $Ca_2YZr_2Al_3O_{12}$:Bi^{3+},Eu^{3+} phosphors. Ceramics International (2020).http://dx.doi.org/10.1016/j.ceramint.2019.11.081

[41] Mo, F. et al. Luminescence of $K_2BaCa(PO_4)_2$: Ce^{3+}, Tb^{3+} dual-emitting phosphor and its application as ratiometric optical thermometer. Ceramics International (2019).http://dx.doi.org/10.1016/j.ceramint.2019.03.147

[42] Qiu, Y., Cui, R., Zhang, M. & Deng, C. Dual-emitting Dy^{3+}/Eu^{3+} co-doped $SrLaGaO_4$ phosphor: Tunable luminescence, energy transfer and ratiometric temperature sensing. Journal of Molecular Structure (2024).http://dx.doi.org/10.1016/j.molstruc.2024.137622

[43] Xu, F. et al. Ratiometric temperature sensing behavior of dual-emitting Ce^{3+}/Tb^{3+} co-doped $Na_5Y_9F_{32}$ single crystal with high relative sensitivity. Journal of Alloys and Compounds (2021).http://dx.doi.org/10.1016/j.jallcom.2021.159790

[44] Li, M., You, F., Liang, C. & He, Z. Ratiometric thermal sensing based on dual emission of YBO_3:Ce^{3+}, Tb^{3+}. Journal of Alloys and Compounds (2020).http://dx.doi.org/10.1016/j.jallcom.2020.155011

[45] Yu, B. et al. Tunable emission and temperature sensing performance in novel oxyfluoride borosilicate glass ceramics containing Eu^{3+}/Tb^{3+}: KY_3F_{10} nanocrystals. Ceramics International (2020).http://dx.doi.org/10.1016/j.ceramint.2020.12.106

Acknowledgments

This work was supported by the Natural Science Foundation of Zhejiang Province, China (No. LQ21A040003) and K.C. Wong Magna Fund in Ningbo University.

Author Statement

Zhushen Jiang: Formal analysis, Writing original draft. Huimin Ding:Visualization. Youjun Cai: Visualization. Kaikai Ren: Visualization. Xin Wang: Visualization. Yuepin Zhang: Conceptualization, Project administration, Supervision.